UC Davis
UC Davis Previously Published Works

Title
Understanding charge transport in donor/acceptor blends from large-scale device simulations based on experimental film morphologies

Permalink
https://escholarship.org/uc/item/35h2n2r6

Journal
Energy & Environmental Science, 13(2)

ISSN
1754-5692

Authors
Li, Haoyuan
Sini, Gjergji
Sit, Joseph
et al.

Publication Date
2020-02-19

DOI
10.1039/c9ee03791h

Peer reviewed

PAPER

Understanding charge transport in donor/acceptor blends from large-scale device simulations based on experimental film morphologies†

Haoyuan Li, [ID] [a] Gjergji Sini, [ID] [ab] Joseph Sit, [ID] [c] Adam J. Moulé [ID] [c] and Jean-Luc Bredas [ID] *[a]

Bulk-heterojunction organic photovoltaic (OPV) devices consist of active layers made of electron donor/acceptor blends. Understanding the impact of the blend morphologies on the optoelectronic processes occurring in OPVs is of crucial importance for a complete description of the device physics and the achievement of higher device efficiencies. However, high-resolution morphology data are scarce and theoretical methodologies with the appropriate level of details and affordable computational costs are underdeveloped. As a result, previous device modeling often had to rely on artificially generated blend morphologies, which do not represent those in actual devices. Here, by considering three-dimensional donor/acceptor blend morphologies recently determined *via* electron tomography, we have established an original approach that allows us to perform device-scale simulations of charge transport in actual blend morphologies. The current characteristics, carrier distributions, and internal current pathways and densities are determined and compared to those based on the artificial morphologies often used in OPV-related studies.

Broader context

Bulk-heterojunction organic photovoltaic (OPV) devices are promising low-cost energy solutions with state-of-the-art efficiencies now exceeding 16%. However, further performance improvements are still needed for practical applications, which requires to better understand the underlying device physics. The relationship between active-layer morphology of binary and ternary blends and device efficiency has many facets that are still largely incomplete; in particular, the connection between morphology and charge transport within the device active layer has remained elusive. Here, we describe an original approach that allows the theoretical simulation of charge transport at the scale of the device, on the basis of reliable morphology data determined *via* electron tomography. As a result, our work provides an in-depth analysis of key elements of the device physics, which incorporates accurate macroscopic and microscopic morphological details. It represents an essential stepping stone towards a comprehensive description of the operation of OPV devices and an important platform in the quest for enhanced organic solar-cell efficiencies.

1. Introduction

Organic photovoltaics (OPVs)[1–4] are promising renewable-energy solutions. Since their initial development in 1986,[5] great

progress in their power conversion efficiencies (PCEs) has been achieved, with state-of-art values now reaching over 16%.[6–12] OPV devices usually consist of organic active layers based on a blend of two components: an electron donor and an electron acceptor material. These two components do neither homogeneously mix into a single phase nor fully separate and the organic layer often has a complex morphology with nonuniform domains at quasi-equilibrium. Since the operation of OPV devices requires hole–electron pairs to separate at donor/acceptor interfaces and the generated charges to transport to the electrodes, the PCEs strongly depend on film morphology. Understanding in detail the impact of film morphology on device performance and being able to control the morphology characteristics are key to further improving OPV efficiencies. Such developments have

[a] School of Chemistry and Biochemistry, Center for Organic Photonics and Electronics (COPE), Georgia Institute of Technology, Atlanta, Georgia 30332-0400, USA. E-mail: jean-luc.bredas@chemistry.gatech.edu

[b] Laboratoire de Physico-chimie des Polymères et des Interfaces, Université de Cergy-Pontoise, 5 Mail Gay Lussac, Neuville sur Oise, Cergy-Pontoise Cedex 95031, France

[c] Department of Chemical Engineering, University of California Davis, CA 95616, USA

This journal is © The Royal Society of Chemistry 2020

Energy Environ. Sci., 2020, **13**, 601–615 | **601**

become increasingly important as state-of-the-art OPV devices are often based on complex molecular structures and film components, both of which are expected to lead to more complex film morphologies.[9,13–15] However, this remains a daunting task[16–20] as it is still extremely challenging to experimentally probe the organic film with a molecular resolution, which is the level of detail needed to describe the optoelectronic processes in an OPV device due to the localized nature of the electronic states in organic materials.[21,22] From a theoretical perspective, while molecular dynamics simulations have been applied successfully to model the local morphology in donor/acceptor blend films,[23–26] the sizes of the modeled systems are often limited to ∼10 nm and thus information on the global morphology, which is essential to calculate accurate device characteristics, cannot be accessed. In practice, device modeling is usually based on an artificial global morphology generated through a simulated phase-separation process with parameters that may not correspond to the actual material.[27–31] This *ad hoc* nature means that previous interpretations of the microscopic processes in bulk-heterojunction OPV devices may not stand on reliable footing. In addition, this approach does not naturally produce a mixed phase, which is expected to play an important role in device operation. Therefore, it is of great importance to be able to go beyond such an approach, which is the main objective of the present work.

Electron tomography (ET) is a recently developed technique that enables the reconstruction of three-dimensional (3D) morphologies starting from a tilt series of two-dimensional (2D) projection images obtained with a scanning transmission electron microscope (STEM).[32,33] ET has been used to characterize the 3D morphologies of donor/acceptor blend films of poly(3-hexylthiophene) (P3HT)/Lu$_3$N@C$_{80}$-PCBEH with a 1–10 nm^3 resolution.[34,35] The heavy Lu atoms increase the contrast between donor and acceptor components and allow one to gain molecular resolution with good precision; this resolution is similar to that obtained in simulated morphologies but comes with significantly improved reliability and scale. This makes such ET-measured morphology data extremely valuable in the characterization of the microscopic processes in OPV devices. At this stage, it is important to bear in mind that: on the one hand, ET measurements remain scarce and are not expected to be integrated into a typical device optimization workflow any time soon; and, on the other hand, the systems under investigation are not expected to provide optimal phase separation. However, our work transcends those issues by providing the first example of correlation between device-scale modeling and actual OPV morphology data.

So far, the interpretation of OPV morphology reconstructions has essentially relied on graph-based methods.[35,36] However, many of the essential features of organic semiconductors, such as the presence of localized electronic states,[21] the hopping nature of charge transport,[22] and the impact of disorder,[22,37] cannot be accounted for with this geometrical approach. To connect these morphology data to device performance on a much more reliable footing, a molecular-level device modeling approach is definitely required.

Molecular-level device modeling has proven to be very useful in the study of organic electronic devices since microscopic processes such as charge-carrier hopping can be fully considered. In this context, the kinetic Monte Carlo (KMC) approach has been the prevalent method of choice; in KMC, microscopic events occur one-by-one and proceed until enough information has been collected.[28–31,38–50] However, applying KMC to devices of sizes beyond ∼100 nm is very difficult since the computational cost increases superlinearly with system size, and even more so when experimentally relevant voltages are considered. Thus, KMC is only feasible when considering slices of the ET-measured morphology one at a time, which can lead to strong finite-size effects and large statistical errors (see the data in ESI†). Recently, we developed an efficient master equation (ME) method that provides a consistent description of both short-range and long-range electrostatic interactions and is able to model diode-structure devices with lateral dimensions up to 1 μm at affordable computational costs.[51] However, the ET-measured morphology data are intrinsically different from the simulated morphologies. As a result, previous device simulation protocols that have been developed for simulated blend morphologies cannot be directly applied to the study of these experimental morphologies. Here, we develop an original approach that allows the first device-scale simulations based on experimental donor/acceptor blend morphologies, in order to determine the charge-transport properties in OPV blends. In particular, we have developed a methodology to process the morphology data required for molecular-level simulations and developed a flexible interface in our master equation simulations to import any arbitrary morphology unaltered. Thus, by integrating the actual-scale film morphology into the device modeling, we are able to perform an in-depth analysis of the device physics. In addition, our approach offers the opportunity to address the validity of the widely used artificial morphologies.

2. Methodologies

2.1 Experimental morphologies

The 3D phase distributions in four organic donor/acceptor blend samples fabricated under different conditions have been previously experimentally characterized with near molecular resolution *via* electron tomography.[35] The first two samples (hereafter labeled **Ia** and **Ib**) were prepared through spin coating, with **Ib** further processed *via* thermal annealing; the third and fourth samples (**Ic** and **Id**) were prepared by blade coating, with **Id** further processed *via* thermal annealing. These data sets cover some of the most widely used experimental conditions in OPV fabrication.[11,18,19] There occur three different phases in these samples: a donor phase, a mixed phase, and an acceptor-rich phase (Fig. 1). Visualizations of cross-sections of these morphologies can be found in Fig. S1–S4 in the ESI.†

The morphology of the donor/acceptor film depends strongly on the preparation conditions, with, for instance, thermally annealed samples consisting of larger domains as compared to non-annealed ones. Thus, it is useful to quantify the domain

602 | *Energy Environ. Sci.*, 2020, **13**, 601–615

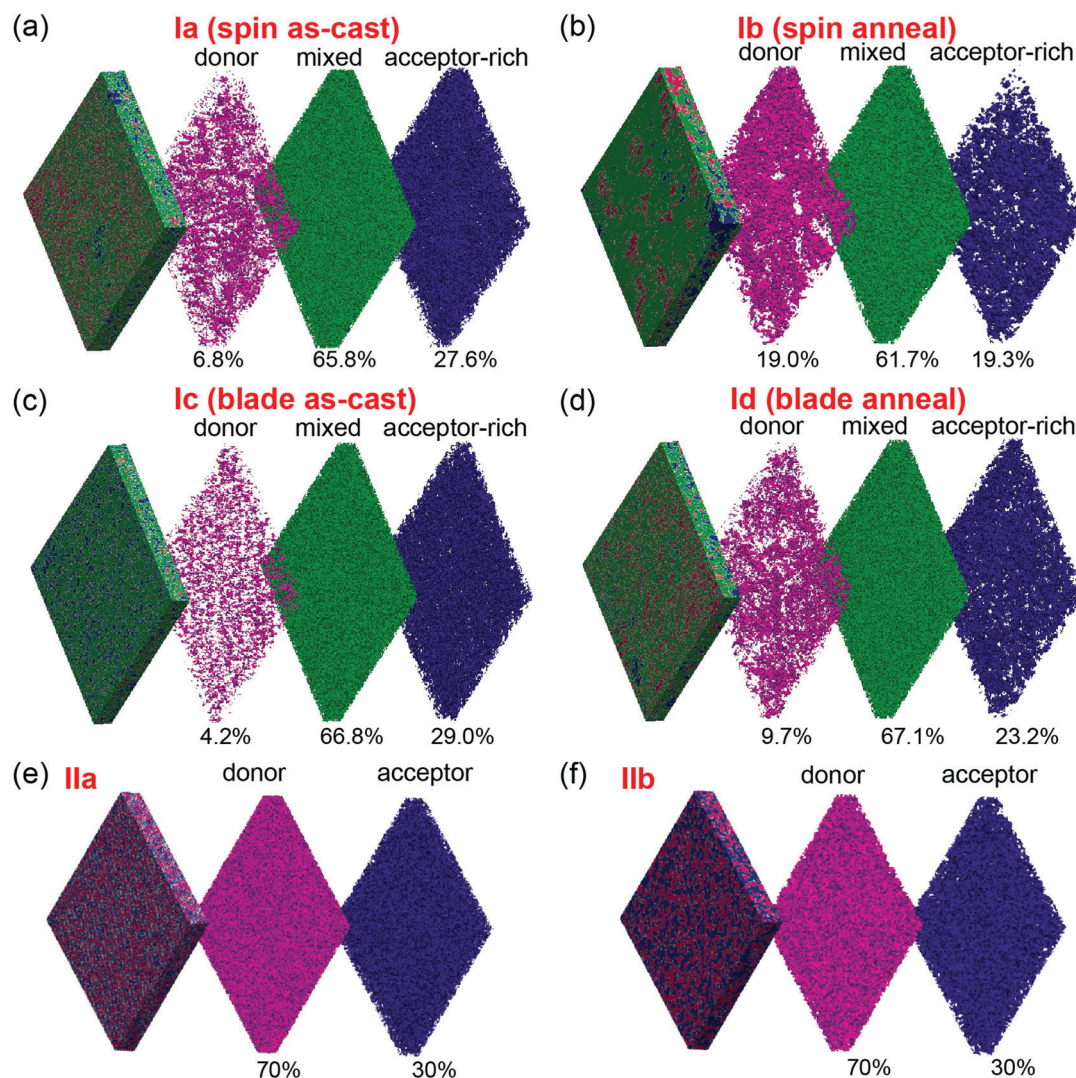This journal is © The Royal Society of Chemistry 2020

Fig. 1 Visualization of the donor/acceptor blend morphologies. (a) **Ia**, (b) **Ib**, (c) **Ic**, and (d) **Id** are experimental morphologies. (e) **IIa** and (f) **IIb** are artificial morphologies from simulated phase separation. The percentages of the volume ratios of the different phases are shown. The film thicknesses from (a) to (f) are 103 nm, 96 nm, 79 nm, 79 nm, 96 nm, and 96 nm, respectively. The lateral dimensions are all 750 nm × 750 nm. The cross-sections of these morphologies can be found in Fig. S1–S6 in the ESI.†

sizes of the different phases in the various morphologies. These can be evaluated by using the interfacial area and the volume of the phase, assuming that voxels are cubic at the limit of resolution and that the interface-to-volume ratio of domains is the same as that of a cube.[52] The approximate domain sizes of the different phases are shown in Table 1. The domain sizes of the donor phase range from 16 to 24 nm, while those of the

acceptor-rich phase range from 18 to 27 nm. The lateral dimensions of these morphologies are all 750 nm × 750 nm; these values are much larger than the domain sizes, which ensures sufficient sampling. The site spacing is 2.4 nm. These morphology data are used as input into the ME simulations with consideration of their actual scale.

2.2 Artificial morphologies

Besides considering the experimental morphologies described in Section 2.1, we also consider artificial morphologies from a simulated phase separation process, as these have been widely adopted when modeling OPV devices.[28–31] The donor : acceptor volume ratio is set as 7 : 3, which is similar to those in samples **Ia–Id**. Two different blends **IIa** and **IIb** were produced, whose morphology data were extracted from a simulated phase separation trajectory (see Section 1 of the ESI† for details). This process naturally generates two phases: a donor phase and an

Table 1 Approximate domain sizes of the different phases

Morphology	Donor phase (nm)	Mixed phase	Acceptor(-rich) phase (nm)
Ia	16	25 nm	19
Ib	24	31 nm	27
Ic	15	24 nm	18
Id	17	27 nm	20
IIa	23	N/A	15
IIb	46	N/A	23

This journal is © The Royal Society of Chemistry 2020

Energy Environ. Sci., 2020, **13**, 601–615 | **603**

acceptor phase. **IIa** has a smaller degree of phase separation, with approximate donor and acceptor domain sizes of 23 nm and 15 nm, respectively (Table 1). **IIb** has a larger degree of phase separation, with approximate donor and acceptor domain sizes of 46 nm and 23 nm, respectively. Visually, the acceptor domain size of **IIb** is close to the acceptor-rich domain size of **Id**, while the acceptor domain size of **IIa** is smaller than that of the acceptor-rich domain size of **Ic** (see Fig. S3–S6 in the ESI†). The lateral size and the site spacing of **IIa** and **IIb** are the same as in the experimental morphologies.

2.3 Microscopic parameters

In order to properly describe charge transport in these blends, information on the individual molecular energy levels at the various sites and the charge-transfer rates are needed. Here, these microscopic parameters are determined from experimental and theoretical data on the donor and acceptor components, whose details can be found in Sections 2 and 3 of the ESI.† In particular, the molecular sites belonging to different phases are assigned to one of the following four categories: crystalline donor (D_{cr}), amorphous donor (D_{amor}), crystalline acceptor (A_{cr}) and amorphous acceptor (A_{amor}). From the experimental morphology data, donors in the donor phase are assessed to be D_{cr}, while those in the mixed and acceptor-rich phases are D_{amor}; acceptors in the acceptor-rich phase are considered as A_{cr}, while those in the mixed phase are A_{amor}, as illustrated in Fig. 2. Experimentally, regiorandom P3HT:PCBM mixtures with PCBM volume ratios less than ~0.6 were found to be fully miscible.[53,54] In our simulations, a molecular-scale mixing is assumed in the mixed phases and the acceptor-rich phases. The molecular sites in these two phases are assigned randomly to one of the D_{amor}, A_{cr}, and A_{amor} categories according to the above rules and the volume ratios (see Table S1 in the ESI†). For the two artificial morphologies considered here, the donor phase is entirely D_{cr} and the acceptor phase is A_{cr}.
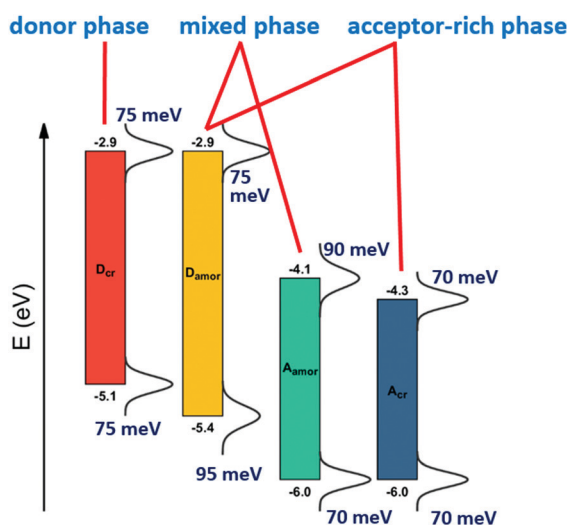

Fig. 2 Illustration of the assignment of organic sites and their energy levels in the master equation simulations.

2.4 Device design

Here, we investigate charge transport by considering single-carrier-type diodes. For each of the morphology data shown in Fig. 1, a virtual hole-only device and a virtual electron-only device are constructed by sandwiching the organic film between two electrodes, which amounts to a total number of 12 devices. For the hole-only devices, the Fermi level (E_F) of the electrode is set to −4.9 eV, a value slightly above the IP level of D_{cr}; for the electron-only devices, the electrode E_F is set to −4.5 eV, which is slightly below the EA of A_{cr}; these settings are chosen in order to minimize the influence of current injection and thus allow us to focus on the charge-transport processes within the organic film.

Lattice sites ($n_x \times n_y \times n_z$) with a spacing of 2.4 nm are used to represent each device. Layers at $z = 1$ and $z = n_z$ correspond to the two electrodes. Layers from $z = 2$ to $z = n_z − 1$ correspond to the organic active layer and are set according to the morphology data and the site-assignment procedure described in Section 2.3.

While experimentally devices are engineered to have current to flow in one direction, it is actually useful to model identical electrodes in the simulations and to consider both forward and backward potentials; this allows us to determine whether the vertical morphology matters in the presence of a vertical concentration gradient in a phase. The applied voltages are chosen to be relevant to OPV device applications;[55,56] we have set the voltages to vary from −1.0 V to +1.0 V, with a 0.05 V interval. While KMC simulations of devices at low voltages are often unfeasible due to demanding computational times, the efficiency of our ME simulations enables us to consider voltage magnitudes as low as 0.05 V. Our simulation results overall correspond to the experimental dark current–voltage measurements.

2.5 Master equation simulations

Our recently improved ME methodologies[51] allow us to model reliably such sub-micron devices as a function of voltage. Each site is associated with an occupation probability p, which evolves according to the following equation:[57–63]

$$\frac{dp_i}{dt} = \sum_{j \neq i} -k_{ij}p_i(1 - p_j) + k_{ji}p_j(1 - p_i) \quad (1)$$

where t represents time. The charge-transfer rates k_{ij} and k_{ji} are evaluated according to the Miller–Abrahams equation.[64] We consider charge transport both within the same class of categories (*e.g.*, from D_{cr} to D_{cr}) and among different categories (*e.g.*, from D_{cr} to D_{amor}). To provide a consistent description of charge transport, hole transport in acceptor molecules and electron transport in donor molecules are allowed but with a small rate (see Section 2 of the ESI† for details). The electric potentials (φ) in the device are solved using the 3D Poisson equation (the relative permittivity ε is set to 4) and the carrier self-interaction error is suppressed.[65]

We note that, in the ME simulations, the carrier densities are not pre-defined but rather correspond to the steady state the system reaches at the specified voltage. The influences of the electric field and carrier density on charge transport are inherently taken into account.

604 | *Energy Environ. Sci.,* 2020, **13**, 601–615

This journal is © The Royal Society of Chemistry 2020

Modeling such large devices with complex morphologies is found to be computationally demanding even in the context of our efficient master equation simulations. The simulation time depends on the morphology data as well as the applied voltage. While some simulations finish within a couple of days, convergence does become increasingly difficult at lower voltages. The simulations were run on computer clusters (Intel Xeon E5-2650 v2 processors) whenever resources were available during a period of 8 months. At that point, most of the simulations were completed, with a few exceptions corresponding to extremely small voltages and for most of the data points of the hole-only device of **Ia** (whose convergence is extremely slow; *e.g.*, the simulation at 1.0 V did not converge even after 82 days of combined wall time).

3. Results and discussion

The master equation simulations give detailed information on the macroscopic current densities as well as the microscopic carrier distributions for different morphologies, which are critical aspects of device function but not typically available in graph-based or analytical approaches. It is thus important that we be able to extract information relevant to device performance from the ME results. In Sections 3.1–3.5, we present an in-depth analysis of the charge mobilities, carrier densities, charge-transport pathways, and recombination aspects.

3.1 Current density–voltage curves and charge-carrier mobilities

The calculated current density–voltage (J–V) curves of the hole-only and electron-only devices are shown in Fig. 3. Among the two artificial morphologies, **IIb**, which has a larger degree of phase separation than **IIa** (46 nm *vs.* 23 nm for donor domains and 23 nm *vs.* 15 nm for acceptor domains), is found to have 20–25% and 50–60% larger current densities for the hole-only and the electron-only devices, respectively. For the experimental morphologies, annealing, which leads to increased phase separation and larger domains, also results in increased current densities but to a larger degree than in the artificial morphologies. For the hole-only devices, both **Ib** and **Id** have 1 order of magnitude higher current densities than **Ia** and **Ic**; for the electron-only devices, **Ib** and **Id** have 50–150% and 70–100% higher current densities than **Ia** and **Ic**, respectively. Overall, these trends are consistent with the reported data on hole-only and electron-only devices of polymer/fullerene blends.[66] In addition, for most of the morphology data, the square root of the current is approximately linear with the applied voltage (see Fig. S11 and S12 in the ESI†), which is in line with the experimental data on polymer/fullerene blend devices[56,66] and reminiscent of the space-charge-limited current (SCLC). The charge mobilities (μ) can thus be fitted according to the Mott–Gurney equation[67] as done in the SCLC measurement and the results are shown in Fig. 4. For the artificial morphologies, **IIb** has slightly larger hole mobilities ($\sim 10^{-4}$ cm^2 V^{-1} s^{-1}) and electron mobilities (3.5×10^{-3} cm^2 V^{-1} s^{-1}) than **IIa**.
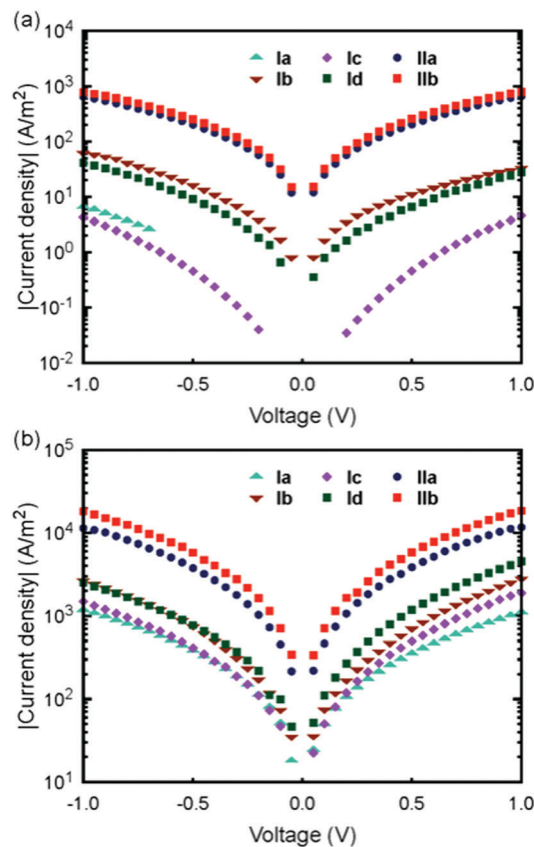

Fig. 3 Calculated current density–voltage curves of (a) hole-only devices and (b) electron-only devices for the different film morphologies. We note that convergence of the hole-only device for **Ia** is extremely slow and only a limited fraction of the data points were obtained.

For the experimental morphologies, both the hole and electron mobilities are nearly one order of magnitude smaller when compared to those obtained for the artificial morphologies, and follow the order: **Ib** (spin anneal) > **Id** (blade anneal) > **Ia** (spin as-cast) > **Ic** (blade as-cast). Therefore, it is seen that a greater phase separation improves charge transport in both the experimental and artificial morphologies. An earlier report based on the geometric, graph-based assessment of samples **Ia**–**Id** suggested that spin-cast films have greater hole transport than blade-cast films and that annealing improves it.[35] We note that these conclusions remain valid in our device-scale ME simulations, in which the molecular energy levels, disorder, and hopping nature of transport are explicitly included.

Overall, these results demonstrate that the device simulation approach developed here, which directly connects the experimental donor/acceptor blend morphology to the macroscopic device characteristics, is indeed reliable.

It is of interest to address the higher hole- and electron mobilities of **IIa**–**IIb** (by 1–2 orders of magnitude) with respect to **Ia**–**Id**. Regarding hole mobility, the smaller volume ratio of the donor phase in **Ia**–**Id** compared to **IIa**–**IIb** can be the explanation (we note that the mixed phase does not transport charge carriers efficiently; see Section 3.2 for details; thus, to a

This journal is © The Royal Society of Chemistry 2020

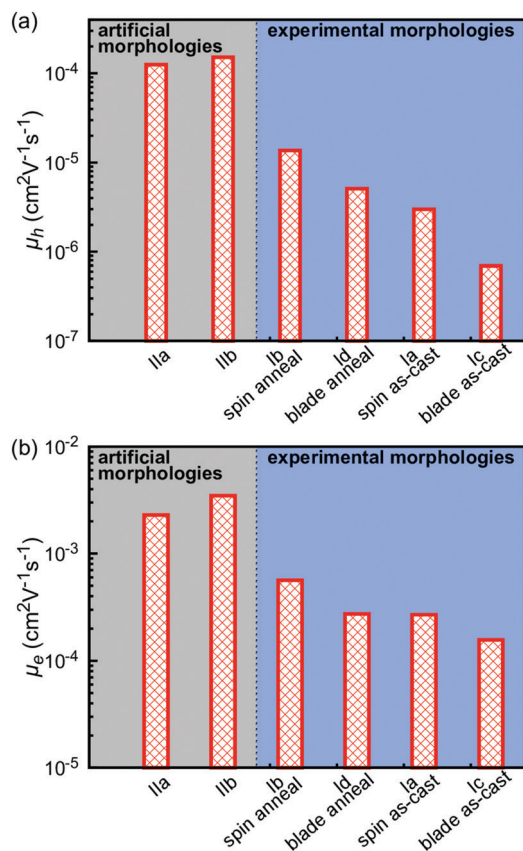*Energy Environ. Sci.,* 2020, **13**, 601–615 | **605**

Fig. 4 (a) Hole and (b) electron mobilities evaluated based on space-charge-limited current theory, using a voltage range from −1.0 V to −0.05 V.

good approximation, in the case of hole transport, the mixed phase can be viewed as an acceptor phase). Indeed, test simulations indicate that reducing the volume ratios of the donor phase in the artificial morphologies leads to smaller mobilities, which is consistent with the evolution of **Ia–Id** as a function of their donor phase ratio (see Fig. S13 in the ESI†). While a similar argument could in part rationalize the smaller electron mobilities determined for the experimental morphologies, the primary explanation is to be found in the lesser purity of the acceptor-rich phases in these morphologies; indeed, further calculations show that reducing the purity of the acceptor phase from 100% to 30% in the artificial morphologies results in 1 order of magnitude lower mobility values (see Fig. S14 in the ESI†).

Thus, the results obtained for the artificial morphologies provide overall similar trends as those for the experimental morphologies: a larger phase volume ratio, a larger domain size, and a purer phase are beneficial to charge transport. However, an important difference arises: compared to the devices based on artificial morphologies, the $|J|$–V curves for the experimental morphologies are more asymmetric in terms of negative vs. positive voltages, as shown in Fig. 3. This originates in the fact that artificial morphologies have overly uniform and isotropic domain distributions, an outcome of the simplified procedure used to generate them, vide infra.

3.2 Carrier densities and charge transport in different phases

The ME simulations give detailed carrier occupations at the various organic sites, which allows us to perform an in-depth analysis of the device physics, an aspect that is not fully accessible in graph-based approaches or analytical methodologies such as drift-diffusion.

We first consider artificial morphologies. In order to focus on the bulk properties, the three organic layers closest to each of the two electrodes (∼7 nm) are excluded from the analysis. Fig. 5 shows the average carrier densities in the different phases for the simulated hole-only and electron-only devices. The holes are found to be entirely located in the donor phase and electrons in the acceptor phase. The average carrier densities are in the range of 10^{16}–10^{17} cm^{-3}, values similar to those measured in P3HT:PCBM OPV devices.[68] As the strength of the applied voltage increases, the average carrier density in the organic film also increases (by 70–100% when going from 0.25 V to 1.0 V). Importantly, similar carrier densities are obtained at negative and positive voltages of identical magnitude, which is consistent with the symmetric nature of the $|J|$–V curves shown in Fig. 3 for these morphologies.

We now focus on the hole-only devices based on the experimental morphologies. We recall that, due to the presence of donor molecules in the mixed phases and the acceptor-rich phases, hole transport in these phases cannot be excluded. Fig. 6 shows the average carrier densities in the various phases for the hole-only devices as a function of voltage for **Ib**, **Ic**, and **Id**. As in the case of artificial morphologies, the carrier densities increase with voltage but there appears asymmetry between negative and positive voltages, as expected from the asymmetric $|J|$–V curves in Fig. 3. The reason can be traced back to the asymmetric vertical segregation of the donor phases, which is discussed below in Section 3.3. In addition, while most holes are located in the donor phases, they are also
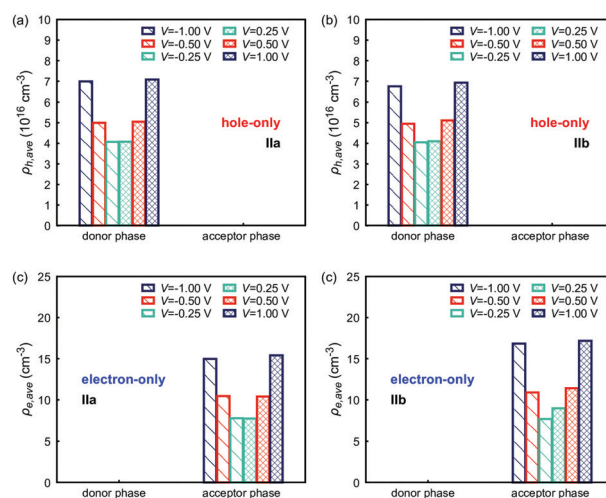

Fig. 5 Average hole densities in the different phases of the hole-only devices for (a) **IIa** and (b) **IIb**; average electron densities in the different phases of the electron-only devices for (c) **IIa** and (d) **IIb**. The three organic layers closest to each of the two electrodes are excluded from the analysis.

606 | Energy Environ. Sci., 2020, **13**, 601–615

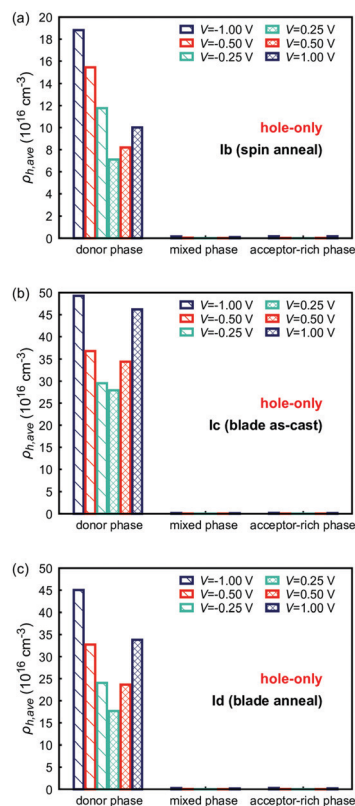This journal is © The Royal Society of Chemistry 2020

Fig. 6 Average hole densities in the various phases of the hole-only devices for (a) **Ib**, (b) **Ic**, and (c) **Id**. The three organic layers closest to each of the two electrodes are excluded from the analysis.
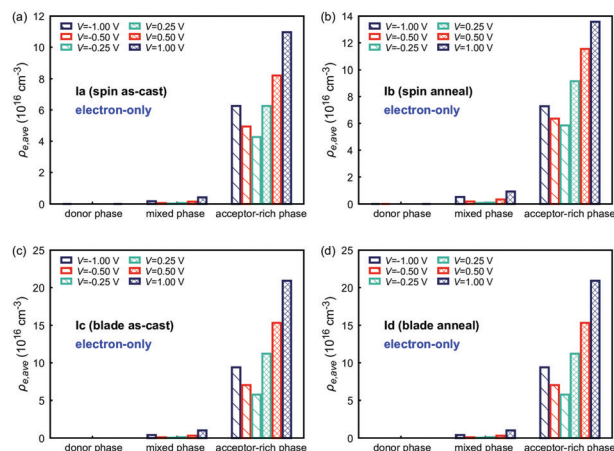

Fig. 7 Average electron densities in the various phases of the electron-only devices for (a) **Ia**, (b) **Ib**, (c) **Ic**, and (d) **Id**. The three organic layers closest to each of the two electrodes are excluded from the analysis.

present in the mixed and acceptor-rich phases. Our analysis shows that their concentrations in these two phases increase with the strength of the applied voltage and goes up to ~4% and ~2%, respectively, within the investigated range of voltage (see Fig. S15 in the ESI†). However, it should be borne in mind that carrier densities do not necessarily translate proportionally into charge transport efficiency.[69] To better quantify carrier motions (current) within different phases or across two of them, we have analyzed the ratio of charge transport in different phases. It is found that holes in the mixed and acceptor-rich phases are less mobile than those in the donor phase. These results can be found in Section 5 of the ESI.†

Fig. 7 shows the average electron densities in the various phases for the electron-only devices of **Ia**, **Ib**, **Ic**, and **Id**. The ratios of electrons in the donor and mixed phases is plotted in Fig. S17 in the ESI.† Fig. 7 and Fig. S17 (ESI†) point to a complete absence of electrons (and hence electron transport) in the donor phase, since it is exclusively comprised of donor molecules. Similar to the case of the hole-only devices, the carrier densities are different at negative and positive voltages of identical magnitude, which again agrees with the asymmetric nature of the $|J|$–V curves calculated for the electron-only devices. In addition, up to over 15% of the total number of electrons can be present in the mixed phase (Fig. S17, ESI†). These electron distributions are more prominent after annealing. However, the electrons in the mixed phase are much less mobile compared to those in the acceptor-rich phase (see Fig. S18, ESI†).

3.3 Vertical carrier-density profiles across the organic film

While the analyses in Section 3.2 give the overall carrier densities in the different phases, carriers are often non-uniformly distributed across the organic film.[70–74] Before discussing the samples studied here, we have simulated the case of a pure donor film as a reference; its vertical hole-density profiles are displayed in Fig. S19 in the ESI.† In this case, the carrier density significantly decreases when moving away from the electrodes and is highest near the injecting electrode. These features are consistent with the earlier results from drift-diffusion and KMC simulations.[70–72] It is important to keep in mind that such vertical variations in hole densities are the result of electrostatic repulsions among the charges and, in the present case, the homogeneous nature of the charge transport medium.

Fig. 8a and b shows the vertical hole-density profiles in the hole-only devices for different voltages across samples **IIa** and **IIb**, along with the vertical concentration of the donor phase. It is worth pointing out that during the simulated phase-separation process, donor molecules tend to aggregate in the center of the film as the majority species, as this lowers the overall energy of the system. As a result, donor [acceptor] molecules have smaller [larger] concentrations close to the electrodes, compared to those in the bulk.

The vertical hole-density profiles of samples **IIa** and **IIb** share many similarities with the pure donor film: the carrier densities are also highest near the injecting electrode and decreases (although to a lesser degree compared to the case of a pure film) when moving away from the electrodes. A similar observation holds true in the case of electron-only devices, which exhibit larger carrier densities near the electrodes. The most noticeable difference between hole-only and electron-only devices is that the curves are less smooth in the electron-only devices, which is likely due to the fluctuations in phase distribution at small volume ratios. We note that suppressing any boundary effect by applying periodic boundary conditions when generating the artificial morphologies leads to more uniform vertical phase concentrations. The characteristics of
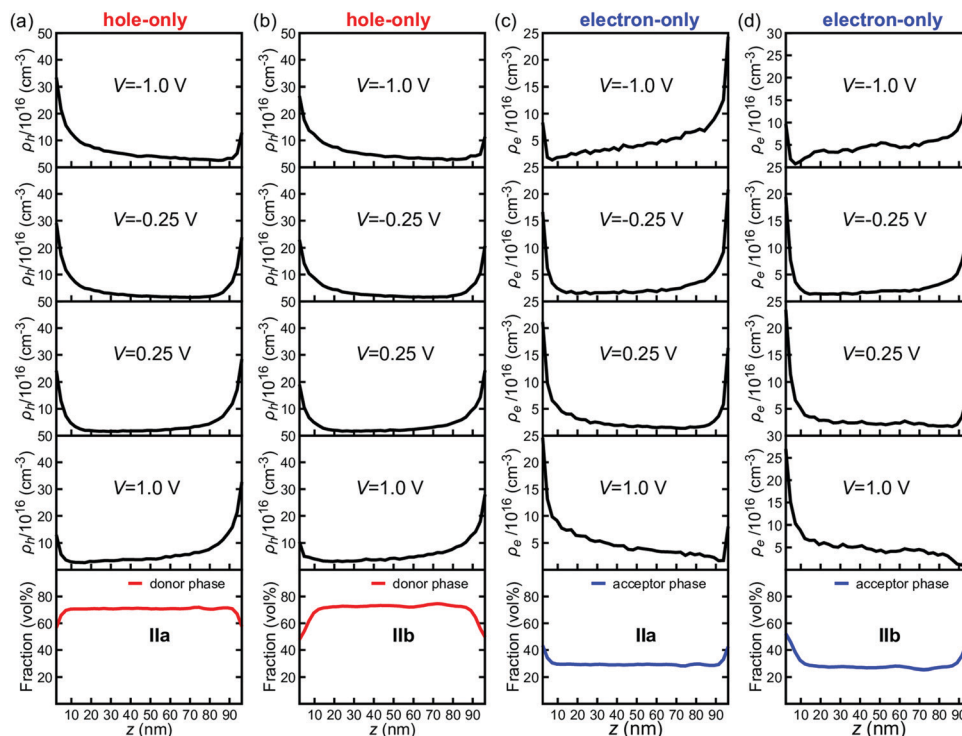
Fig. 8 Vertical hole-density profiles in the hole-only devices at different voltages for (a) **IIa** and (b) **IIb** along with the vertical concentration of the donor phase; vertical electron-density profiles in the electron-only devices at different voltages for (c) **IIa** and (d) **IIb**, along with the vertical concentration of the acceptor phase.

the vertical carrier-density profiles for the artificial morphologies generated under these conditions turn out to be close to those of **IIa** and **IIb** (see Fig. S20 in the ESI†). This indicates that the charge-transport medium has a uniform nature in terms of charge transport and the vertical carrier-density profiles are thus dominated by the electrostatic interactions coming from the external electric field and the coulombic forces among charge carriers.

The results for the experimental morphologies come out to be very different. Fig. 9 shows the vertical hole-density profiles at various positions in the organic film as a function of voltage for **Ib**, **Ic**, and **Id**. The donor phase contributes to nearly all of the hole densities in the organic layer, which is consistent with the results in Fig. 6. However, the vertical hole-density profiles are much more irregular compared to those for the donor-only film and the artificial morphologies. As indicated by test simulations (see Fig. S22 in the ESI† for details), this large difference is not caused by differences in the volume ratios of their donor phases. Since holes are transported mainly in the donor phase, the vertical hole-density profile is significantly impacted by the vertical concentration in the donor phase.

In the experimental morphologies, the vertical concentration of the donor phase is much more inhomogeneous than in the artificial morphologies, a feature illustrated in Fig. 9. As a result, the vertical hole-density profiles are also much less uniform. A decrease in the concentration of the donor phase leads to a lesser volume available for charge transport and thus holes trying to reach the electrodes suffer from increased dead
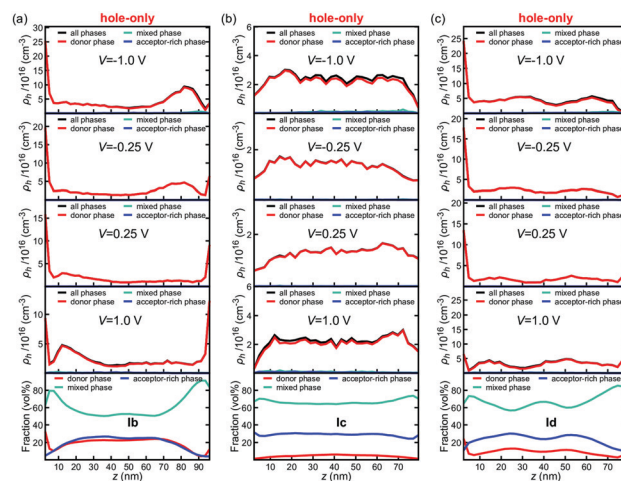

Fig. 9 Vertical hole-density profiles with contributions from different phases in the hole-only devices at different voltages for (a) **Ib**, (b) **Ic**, and (c) **Id** along with the vertical concentrations of different phases. The vertical hole-density profile at −1.0 V for **Ia** can be found in Fig. S21 (ESI†).

ends and scattering. Holes accumulate consequently at places where large variations in the donor phase fraction occur, as Fig. 9a and c illustrate. Notably, **Ic** has the lowest carrier densities (about 50% lower than those of **Ib** and **Id**) among the three morphologies and its carrier density near the electrodes is lower than in the bulk. This low carrier density can be attributed to the lower fraction of the donor phase near the
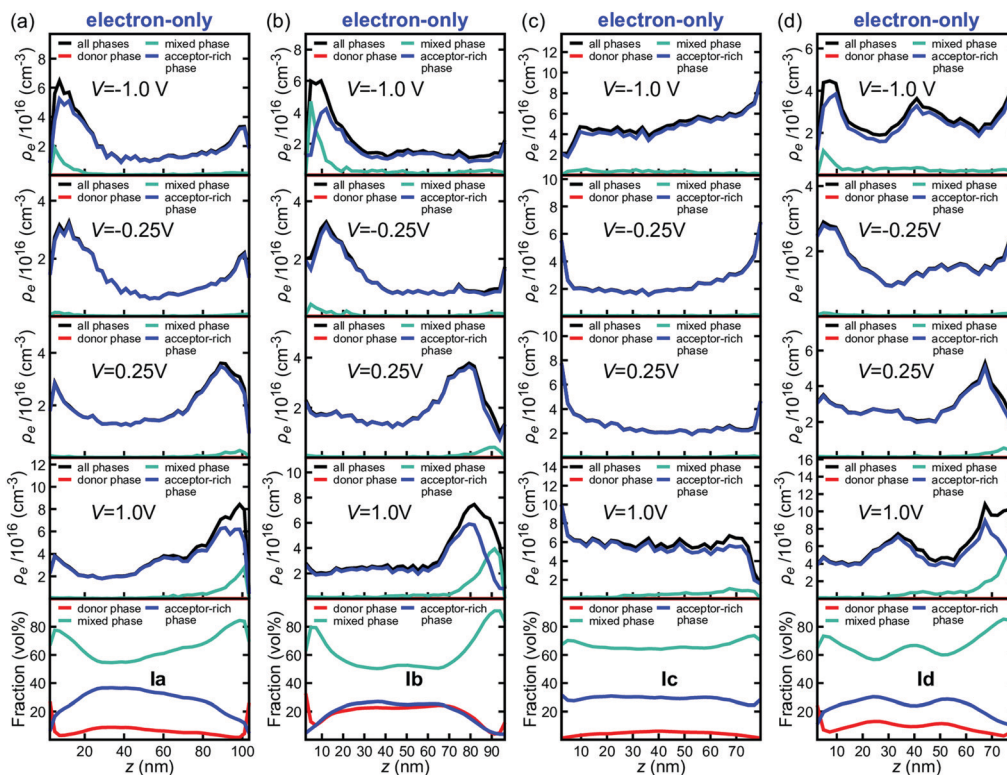
608 | Energy Environ. Sci., 2020, **13**, 601–615

This journal is © The Royal Society of Chemistry 2020

Fig. 10 Vertical electron-density profiles with contributions from different phases in the electron-only devices at different voltages for (a) **Ia**, (b) **Ib**, (c) **Ic**, and (d) **Id** along with the vertical concentrations of different phases.

electrodes, which leads to a barrier to charge injection into the bulk. Indeed, the calculated current/voltage characteristics deviate from the SCLC behavior valid for a uniform morphology film, as shown in Fig. S12 in the ESI.†

The vertical concentration variation of the acceptor(-rich) phase is similarly expected to significantly impact the vertical electron-density profile in the film. Since the vertical concentrations of the acceptor-rich phases are also less uniform in the experimental morphologies, their vertical electron-density profiles are rougher, which is apparent from Fig. 10. In a way comparable to the situation in hole-only devices, electrons tend to accumulate where large variations occur in the acceptor-rich phase fraction. However, in contrast, there appears a larger electron percentage in the mixed phase. This phenomenon is more prominent at high voltages and near the electrodes in **Ia**, **Ib**, and **Id**, where the fraction of the acceptor-rich phase decreases. In these cases, the mixed phase is expected to mediate charge injection from the electrode to the bulk acceptor-rich phase.

The vertical segregation in donor and acceptor-rich phases is unavoidable due to the anisotropic nature of the microenvironment and the variations in local energy landscape.[34,36,75–77] However, these factors are not taken into account in the conventional procedures followed to generate the donor/acceptor blend morphologies used in OPV device modeling. As a result, the artificially generated morphologies produce results that are qualitatively and quantitatively different from the actual morphologies. This is the reason why, while such simulated

morphologies can reproduce aspects of the impact of phase volume fraction, phase purity, and domain size on the electrical properties, they are unable to generate comparable morphological features that would allow a comprehensive comparison of simulation results to experimental data or a fully reliable prediction of materials properties.

3.4 Internal currents

A great advantage of the master equation simulations is that they provide information on the internal currents (from a given site to its neighbor), which can be used to determine in detail the charge-transport pathways in the device. Since the whole device is actually too large for complete visualization, sub-volumes of about 1/100 of the total volume were visualized sequentially. It also turns out to be useful to show only internal currents larger than a given threshold value, $I_{\text{threshold}}$, which is defined as the macroscopic current of the device divided by the number of sites in the lateral plane and by the volume ratio of the donor phase (for hole transport) or the acceptor(-rich) phase (for electron transport). The internal currents satisfying this criterion represent the effective components of the charge-transport network. In the case of nearly uniform charge transport, all internal currents would be around $I_{\text{threshold}}$ and thus half of them would be plotted; they would distribute uniformly over half the available space. In the extreme case of highly inhomogeneous charge transport, on the other hand, only a few internal currents corresponding to the most efficient charge-transport pathways would appear.
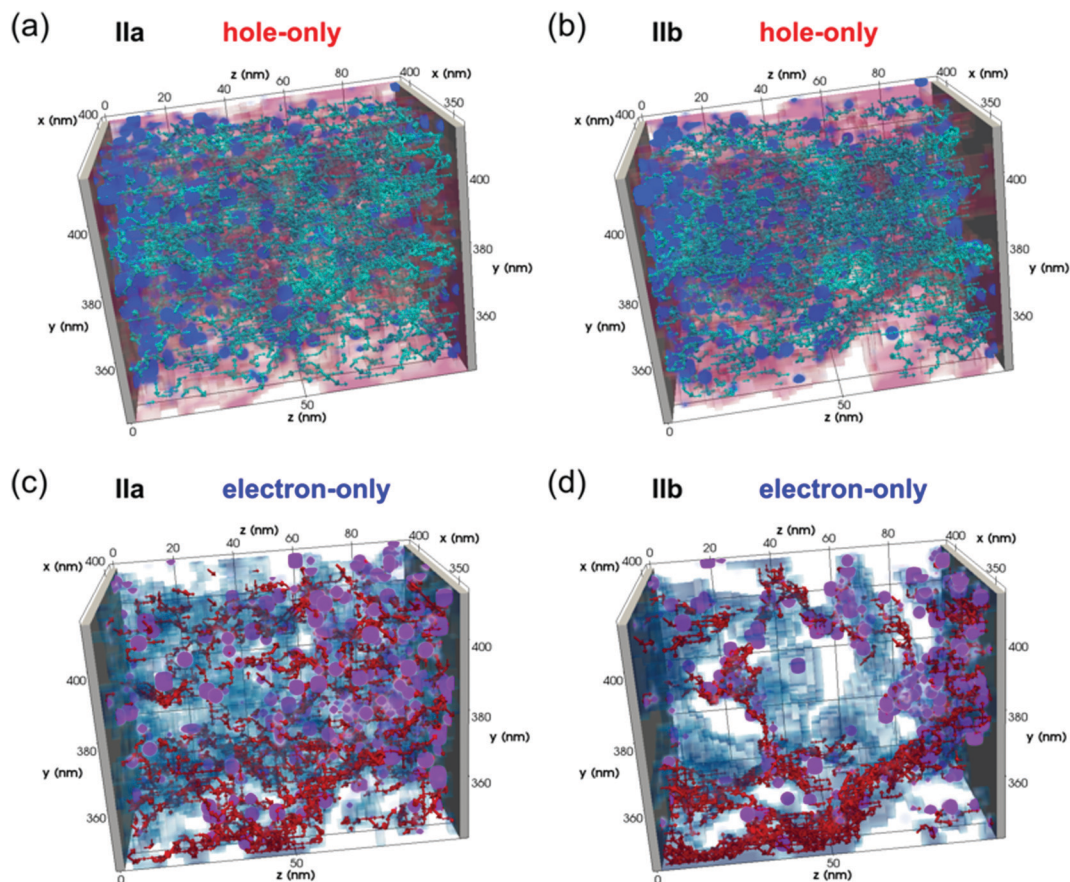
This journal is © The Royal Society of Chemistry 2020

Energy Environ. Sci., 2020, **13**, 601–615 | **609**

Fig. 11 Internal currents in the device central regions (along x and y directions) of the hole-only devices for (a) **IIa** and (b) **IIb**. Red represents the donor phase. Blue represents hole occupations larger than 0.01. Cyan arrows point to internal currents with values higher than $I_{threshold}$ (5.40 × 10^{-15} A and 6.56 × 10^{-15} A, respectively). Internal currents in the central regions of the electron-only devices for (c) **IIa** and (d) **IIb**. Blue represents the acceptor phase. Purple represents electron occupations larger than 0.01. Red arrows point to the internal currents with values higher than $I_{threshold}$ (2.20 × 10^{-14} A and 3.52 × 10^{-13} A, respectively). Gray represents the two electrodes. The voltage is −1.0 V in all cases. High-resolution plots are shown in Fig. S26 (ESI†). Visualizations using different cutoffs can be found in Fig. S27 (ESI†). We note that each subplot corresponds to 1/100 of the whole device.

Fig. 11a and b display the device central regions (along x and y directions) in the hole-only devices of **IIa** and **IIb**. Each frame shows (i) the internal currents satisfying the criterion defined above at −1.0 V; (ii) the hole occupations; and (iii) the donor phase. Holes have larger densities near the injecting electrode (left side) and the distribution of the internal currents (hence, the charge-transport pathways) is more uniform. Fig. 11c and d show the internal currents larger than $I_{threshold}$ in the electron-only devices of **IIa** and **IIb** at −1.0 V. In this case, electron transport is seen to be limited to the acceptor phase. The internal-current distribution is less uniform compared to those in Fig. 11a and b, which is mainly attributed to the different volume ratios of the donor and acceptor phases, as indicated by our test simulations in Fig. S24 and S25 of the ESI.† In addition to Fig. 11, we have also generated a plot using a constant cutoff for the internal currents that allows the comparison of the relative strengths of the charge-transport pathways (see Fig. S27 in the ESI†). Interestingly, we find that increasing the domain size leads to denser currents.

In comparison, the domain distributions and internal currents for the experimental morphologies are both less uniform.

Fig. 12 displays the internal currents larger than $I_{threshold}$ in the middle regions of the hole-only devices for **Ia**, **Ib**, **Ic**, and **Id**. The donor phase distributions in space are more irregular and there are fewer currents larger than $I_{threshold}$ compared to those in Fig. 11a and b, which indeed point to less uniform hole-transport pathways. The difference in the distribution of internal currents in Fig. 11a, b and 12 highlights the impact of the morphology data in the device physics. One reason for this difference can be attributed to the reduced volume fraction of the donor phase (compare Fig. 11a and b and our test calculations in Fig. S24 and S25 of the ESI†). However, the artificial morphologies for both large and small volumes of the donor phase consist of more uniform domains than those in **Ia–Id**; this difference is another origin for the more uniform hole transport found for the artificial morphologies. The fact that the charge-transport network is more uniform in the artificial morphologies points to overestimations of the charge-collection efficiency in previous OPV simulations.[28] Another interesting feature of Fig. 12 is that it shows current flow outside of the donor phase (see regions highlighted by red circles), which suggests that the mixed and acceptor-rich phases do contribute to the hole-transport network.
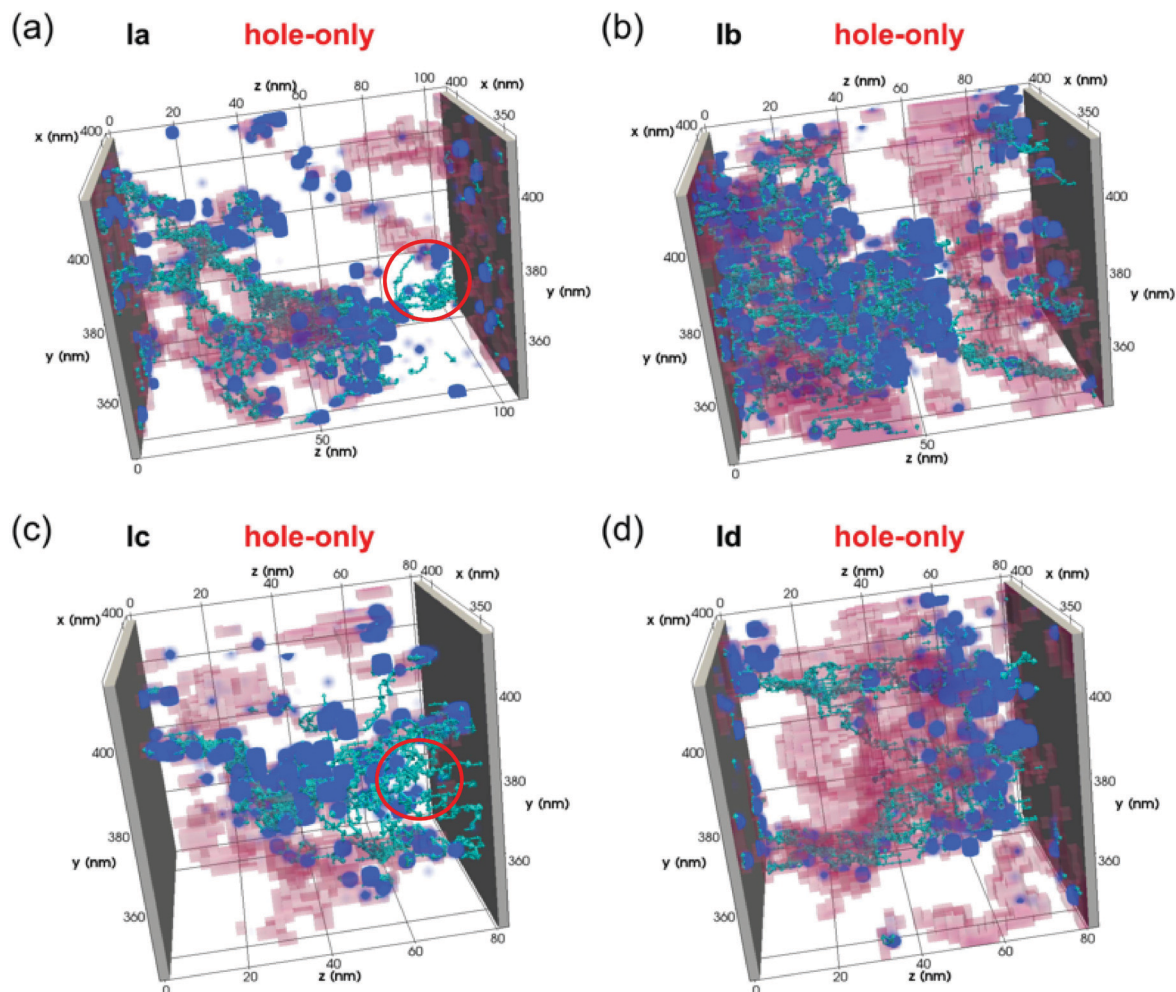
610 | *Energy Environ. Sci.*, 2020, **13**, 601–615

This journal is © The Royal Society of Chemistry 2020

Fig. 12 Internal currents in the central regions (along x and y directions) of the hole-only devices for (a) **Ia**, (b) **Ib**, (c) **Ic**, and (d) **Id**. Red represents the donor phase. Blue represents hole occupations larger than 0.01. Cyan arrows show the internal currents with values higher than $I_{threshold}$ (5.52×10^{-16} A, 1.93×10^{-15} A, 5.91×10^{-16} A and 2.48×10^{-15} A, respectively). Red circles highlight representative regions that currents flow outside the donor phase. The voltage is -1.0 V in all cases. High-resolution plots are shown in Fig. S28 (ESI†). Visualizations using different cutoffs can be found in Fig. S29 (ESI†). We note that each subplot corresponds to 1/100 of the whole device.

Fig. 13 illustrates the internal currents larger than $I_{threshold}$ in the middle regions of the electron-only devices for **Ia**, **Ib**, **Ic**, and **Id**. The electron-transport pathways in the as-cast films **Ia** and **Ic** are relatively uniform. In contrast, those in the annealed films **Ib** and **Id** are less so and are also less homogeneous than those in **IIa** and **IIb**. The domains are visually different in these two kinds of morphologies. The artificially generated morphologies tend to form continuous phases with relatively uniform domain sizes, while the actual morphologies have more discontinuous phases and larger variations in domain size. In addition, electron transport outside the acceptor-rich phase is also observed, which highlights the contribution from the mixed phase.

Overall, these results highlight the fundamental differences between the artificial and experimental morphologies. The artificial morphologies are generated within an idealized procedure that produces too uniform domains, continuous phases, and hence relatively homogeneous charge-transport networks. In fact, an actual organic film has variations in domain sizes and

characteristics, which cannot be reproduced by the artificial morphologies. Thus, the results of simulations of the microscopic processes based on an artificial morphology have to be taken with much caution as they may not represent those in actual OPV devices.

There are several other important findings coming from the experimental morphologies, which we summarize here (more details and discussion of these results can be found in Section 6 of the ESI†): (i) we have identified lateral segregations in the density of charge-transport pathways in **Ia–Id**, which are not entirely consistent with the distribution of the donor phase (for hole transport) or acceptor-rich phase (for electron transport), particularly in the annealed samples. This mismatch points to opportunities for optimizations of the morphologies in order to improve device performance. (ii) The charge-transport networks evolve with applied voltage However, the internal currents do not depend linearly on voltage. While increasing the strength of the applied voltage leads overall to a larger
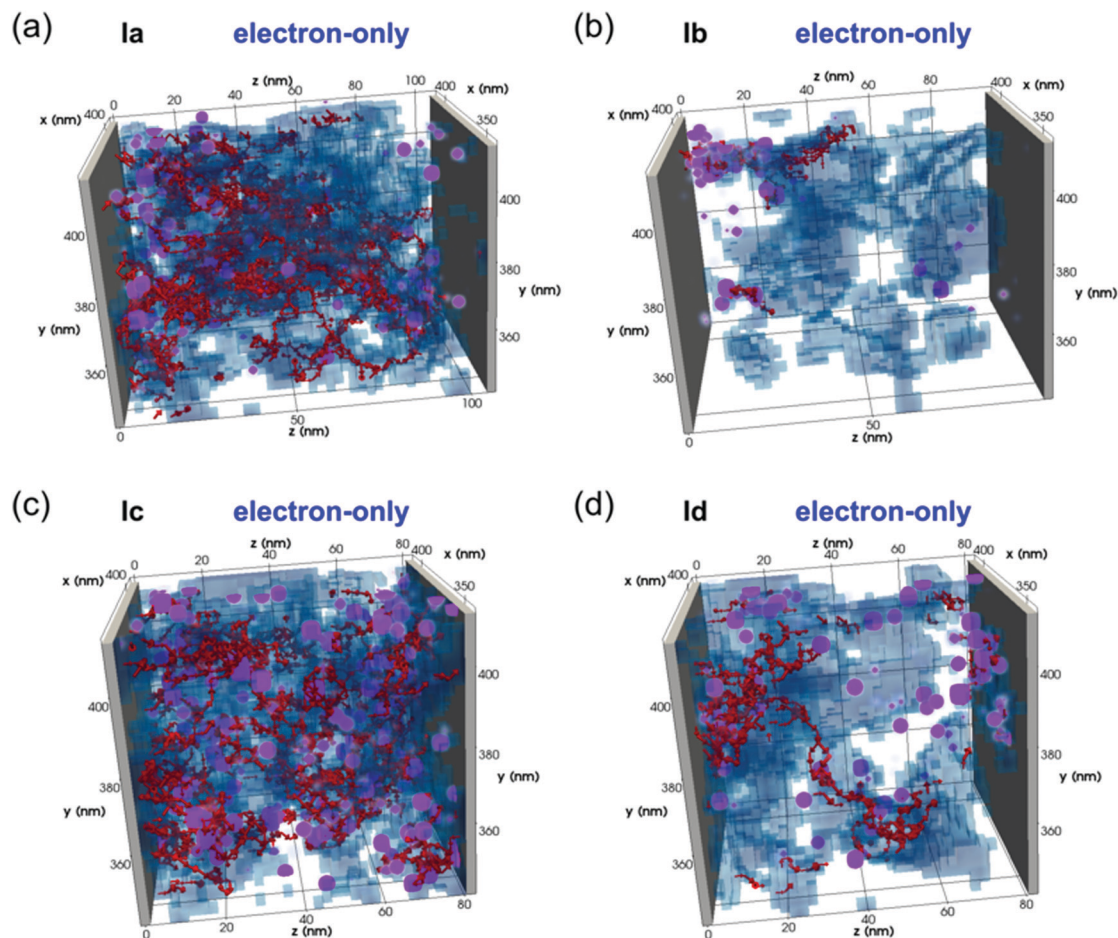
Fig. 13 Internal currents in the central regions (along x and y directions) of the electron-only devices for (a) **Ia**, (b) **Ib**, (c) **Ic**, and (d) **Id**. Blue represents the acceptor phase. Purple represents electron occupations larger than 0.01. Red arrows show the internal currents with values higher than $I_{threshold}$ (2.45×10^{-14} A, 8.14×10^{-14} A, 2.97×10^{-15} A and 6.25×10^{-14} A, respectively). Gray represents the two electrodes. The voltage is -1.0 V in all cases. High-resolution plots are shown in Fig. S30 (ESI†). Visualizations using different cutoffs can be found in Fig. S31 (ESI†). We note that each subplot corresponds to 1/100 of the whole device.

magnitude of charge transport, the internal currents on a local scale can also be weakened (as there appear fewer charge-transport pathways per unit volume). (iii) The charge-transport networks at voltages of identical strength but opposite in sign can be very different.

3.5 Non-geminate recombinations

Based on the simulated hole-only and electron-only devices, it is also possible to gain some information about non-geminate recombination, which is one of the major loss mechanisms that reduce the short-circuit currents, open-circuit voltage, and fill factor in OPV devices.[78] In order to model the recombination process, we consider the volume overlap for holes in hole-only devices and electrons in electron-only devices, for the same morphology and at the same applied voltage. Here, holes and electrons that have a high probability to recombine during OPV operation were identified using a 5 nm cutoff distance (the energy required to escape the Coulomb force at this distance is $\sim$70 meV). The spatial overlap between a hole and electron in the film is thus taken as directly proportional to the

probability of non-geminate recombination in these areas. We note that to minimize the impact of carriers injected from the electrodes on the evaluated hole and electron overlap, the first three organic layers ($\sim$7 nm) closest to the electrodes are excluded from the analysis.

As can be seen in Fig. 14 in the case of **IIa**, up to 25% of the charge carriers come across one another. A larger phase separation reduces this value, with the probability coming down to 16% for **IIb**. This trend is consistent with the results from earlier KMC simulations of OPV devices.[28,31] For the experimental morphologies, the holes and electrons also meet to a lesser extent in the annealed samples **Ib** and **Id** than in their corresponding as-cast samples **Ia** and **Ic**. We note from Fig. 14 that the hole–electron encounter probabilities in the experimental morphologies are less than 4% (*i.e.*, 80–90% lower than those in artificial morphologies), which is very small; this suggests that if the charge carriers generated in the mixed phase are able to enter the donor phase (for holes) or the acceptor-rich phase (for electrons), their probability to be collected at the electrodes can be expected to be high. This also implies that
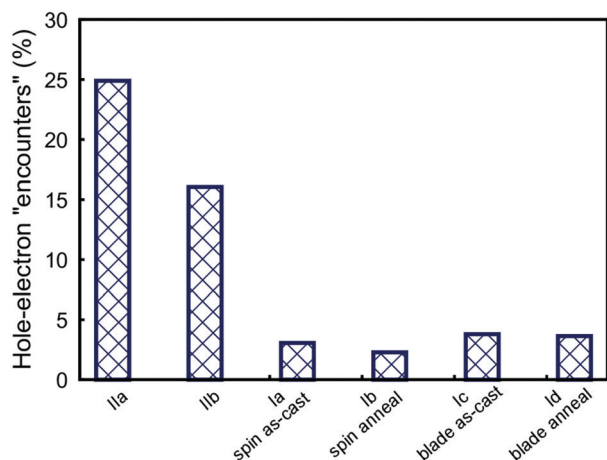
612 | *Energy Environ. Sci.*, 2020, **13**, 601–615

This journal is © The Royal Society of Chemistry 2020

Fig. 14 Ratio of holes and electrons that can meet evaluated from the locations of carriers in the hole-only and electron-only devices at −1.0 V. The first three organic layers closest to the electrodes are excluded from the analysis.

non-geminate recombination mainly occurs in the mixed phase. This is a consequence of the donor phase and the acceptor-rich phase not being in direct contact but rather separated by the mixed phase.[36]

4. Conclusions

In summary, we have developed an original approach to perform molecular-level device simulations based on: (i) experimental morphologies of donor/acceptor blend films of sub-micron sizes determined by electron tomography (ET); and (ii) recently developed master equation (ME) simulation methodologies that enable the reliable modeling of macroscopic devices at experimentally relevant voltages and carrier densities. The calculated current characteristics and charge mobilities provide a detailed rationalization of previously reported experimental data and are overall consistent with earlier assessment of the ET morphology data by graph-based methodologies.

This new approach has allowed us to perform an in-depth analysis of the device physics of single-carrier-type diodes of donor/acceptor blend films based on accurate macroscopic and microscopic morphological details, which is an important stepping stone towards a complete description of OPV operation. On the one hand, device-scale simulations based on reliable morphology data provide new and improved understandings on the charge-transport and recombination features in donor/acceptor blends. On the other hand, a comparison between the results based on different types of morphologies has offered us the opportunity to assess the validity of donor/acceptor morphologies artificially generated from simulated phase-separation processes; the latter have been the prevalent theoretical model systems used in OPV device simulations to date.

The main conclusions we have reached by investigating four experimental morphologies (corresponding to spin-cast or blade-cast films, further annealed or not) are as follows:

(i) Among the three phases determined by ET for each of the films, holes and electrons are mainly present in the donor phase and the acceptor-rich phase, respectively. However, there are significant probabilities of finding hole and electron in the mixed phase (up to 4% and 15%, respectively) with these values voltage-dependent. The charges in the mixed phase are found to be less mobile compared to holes in the donor phase or electrons in the acceptor-rich phase.

(ii) The vertical carrier-density profiles have irregular shapes and large variations for the four investigated samples (which vary according to whether the films are spin-cast or blade-cast and further annealed or not). Carriers accumulate where there occurs a large variation in the vertical concentration of the donor phase (for holes) or the acceptor-rich phase (for electrons); this originates in irregular and asymmetric vertical concentrations of phases.

(iii) The charge-transport networks are highly nonuniform and there occurs lateral segregation of the charge-transport pathways; their characteristics vary among the four films. In addition, the charge-transport networks evolve with applied voltage. However, increasing the voltage does not always lead to denser charge-transport pathways on a local scale.

(iv) The mixed phase plays an insulating role with respect to carriers present in the donor phase and the acceptor-rich phase, which has the positive consequence of preventing their recombination and enhancing the probability of their collection at the electrodes. Since non-geminate recombination is expected to occur mainly in the mixed phase, future optimization to reduce this loss process should focus on this phase.

We can draw the following conclusions from the comparison between the results based on the experimental and artificial morphologies:

(v) While the results based on artificial morphologies are consistent with the trend that larger domains improve hole and electron transport and reduce non-geminate recombination, the phases appearing in the artificial morphologies are more homogeneously distributed due to the lack of inclusion of realistic micro-environmental factors. This higher extent of homogeneity leads to features that are substantially different from those obtained on the basis of the experimental morphologies: (a) charge transport is found to be independent of the direction of applied electric field; (b) the vertical carrier-concentration profiles are similar to that in a single-component film; and (c) the charge-transport networks are more uniform than those present in the experimental morphologies.

(vi) The absence of a mixed phase in the widely used artificial morphologies can lead to charge-transport and recombination features that are at odds with those observed in an actual bulk-heterojunction device.

Taking (v) and (vi) together means that the artificial morphologies cannot provide an accurate interpretation of the optoelectronic processes in bulk-heterojunction OPVs devices. They should thus be considered with much caution. The results in previous simulations that relied on artificial morphologies may need to be reexamined.

We emphasize that donor/acceptor blend morphologies are expected to strongly depend on the molecular structure and

This journal is © The Royal Society of Chemistry 2020

Energy Environ. Sci., 2020, 13, 601–615 | 613

film preparation conditions. While the four films we considered represent polymer/fullerene systems under solution processing conditions, our methodology can also be applied to the study of other systems, such as those based on recently developed non-fullerene small-molecule acceptors and ternary blends.[9,13–15] In addition, we expect that the theoretical tools developed in this work and our approach that combines molecular-level simulations with high-accuracy experimental data, will be valuable in future works that focus on simulation-guided material design and device optimizations.

Finally, while our work focused on charge transport, a full description of OPV operation requires to include simultaneously holes, electrons, and excitons. The methodology we established here form a robust basis to access such a comprehensive description, which is part of our ongoing work.

Conflicts of interest

There are no conflicts to declare.

Acknowledgements

Notes and references

1 A. Mishra and P. Bauerle, *Angew. Chem., Int. Ed.*, 2012, **51**, 2020–2067.

2 Y. Z. Lin, Y. F. Li and X. W. Zhan, *Chem. Soc. Rev.*, 2012, **41**, 4245–4272.

3 J. Hou, O. Inganäs, R. H. Friend and F. Gao, *Nat. Mater.*, 2018, **17**, 119.

4 T. Kirchartz and U. Rau, *Adv. Energy Mater.*, 2018, **8**, 1703385.

5 C. W. Tang, *Appl. Phys. Lett.*, 1986, **48**, 183–185.

6 Y. Cui, H. Yao, B. Gao, Y. Qin, S. Zhang, B. Yang, C. He, B. Xu and J. Hou, *J. Am. Chem. Soc.*, 2017, **139**, 7302–7309.

7 Y. Cui, H. Yao, C. Yang, S. Zhang and J. Hou, *Acta Polym. Sin.*, 2018, 223–230.

8 H. Zhang, H. Yao, J. Hou, J. Zhu, J. Zhang, W. Li, R. Yu, B. Gao, S. Zhang and J. Hou, *Adv. Mater.*, 2018, **30**, 1800613.

9 Y. Lin, J. Wang, Z.-G. Zhang, H. Bai, Y. Li, D. Zhu and X. Zhan, *Adv. Mater.*, 2015, **27**, 1170–1174.

10 Y. Cui, H. Yao, J. Zhang, T. Zhang, Y. Wang, L. Hong, K. Xian, B. Xu, S. Zhang, J. Peng, Z. Wei, F. Gao and J. Hou, *Nat. Commun.*, 2019, **10**, 2515.

11 O. Inganäs, *Adv. Mater.*, 2018, **30**, 1800388.

12 H. Sun, T. Liu, J. Yu, T.-K. Lau, G. Zhang, Y. Zhang, M. Su, Y. Tang, R. Ma, B. Liu, J. Liang, K. Feng, X. Lu, X. Guo, F. Gao and H. Yan, *Energy Environ. Sci.*, 2019, **12**, 3328–3337.

13 D. Baran, R. S. Ashraf, D. A. Hanifi, M. Abdelsamie, N. Gasparini, J. A. Rohr, S. Holliday, A. Wadsworth, S. Lockett, M. Neophytou, C. J. M. Emmott, J. Nelson, C. J. Brabec, A. Amassian, A. Salleo, T. Kirchartz, J. R. Durrant and I. McCulloch, *Nat. Mater.*, 2017, **16**, 363–369.

14 R. Yu, H. Yao, Y. Cui, L. Hong, C. He and J. Hou, *Adv. Mater.*, 2019, **31**, 1902302.

15 T. Yan, W. Song, J. Huang, R. Peng, L. Huang and Z. Ge, *Adv. Mater.*, 2019, **31**, 1902210.

16 S. M. Ryno, M. K. Ravva, X.-K. Chen, H. Y. Li and J.-L. Brédas, *Adv. Energy Mater.*, 2017, **7**, 1601370.

17 L. Ye, B. A. Collins, X. Jiao, J. Zhao, H. Yan and H. Ade, *Adv. Energy Mater.*, 2018, **8**, 1703058.

18 H. Lee, C. Park, D. H. Sin, J. H. Park and K. Cho, *Adv. Mater.*, 2018, **30**, 1800453.

19 A. Wadsworth, Z. Hamid, M. Bidwell, R. S. Ashraf, J. I. Khan, D. H. Anjum, C. Cendra, J. Yan, E. Rezasoltani, A. A. Y. Guilbert, M. Azzouzi, N. Gasparini, J. H. Bannock, D. Baran, H. Wu, J. C. de Mello, C. J. Brabec, A. Salleo, J. Nelson, F. Laquai and I. McCulloch, *Adv. Energy Mater.*, 2018, **8**, 1801001.

20 L. Ye, H. Hu, M. Ghasemi, T. Wang, B. A. Collins, J.-H. Kim, K. Jiang, J. H. Carpenter, H. Li, Z. Li, T. McAfee, J. Zhao, X. Chen, J. L. Y. Lai, T. Ma, J.-L. Bredas, H. Yan and H. Ade, *Nat. Mater.*, 2018, **17**, 253–260.

21 J. L. Bredas, J. E. Norton, J. Cornil and V. Coropceanu, *Acc. Chem. Res.*, 2009, **42**, 1691–1699.

22 V. Coropceanu, J. Cornil, D. A. da Silva, Y. Olivier, R. Silbey and J. L. Brédas, *Chem. Rev.*, 2007, **107**, 926–952.

23 T. Wang, X.-K. Chen, A. Ashokan, Z. Zheng, M. K. Ravva and J.-L. Brédas, *Adv. Funct. Mater.*, 2018, **28**, 1705868.

24 T. Wang and J.-L. Brédas, *Adv. Funct. Mater.*, 2019, **29**, 1806845.

25 G. Han, Y. Guo, X. Ma and Y. Yi, *Sol. RRL*, 2018, **2**, 1800190.

26 G. Han, Y. Guo, X. Song, Y. Wang and Y. Yi, *J. Mater. Chem. C*, 2017, **5**, 4852–4857.

27 P. Peumans, S. Uchida and S. R. Forrest, *Nature*, 2003, **425**, 158–162.

28 P. K. Watkins, A. B. Walker and G. L. B. Verschoor, *Nano Lett.*, 2005, **5**, 1814–1818.

29 R. A. Marsh, C. Groves and N. C. Greenham, *J. Appl. Phys.*, 2007, **101**, 083509.

30 C. Deibel, T. Strobel and V. Dyakonov, *Phys. Rev. Lett.*, 2009, **103**, 036402.

31 M. C. Heiber, C. Baumbach, V. Dyakonov and C. Deibel, *Phys. Rev. Lett.*, 2015, **114**, 136602.

32 B. Goris, T. Roelandts, K. J. Batenburg, H. H. Mezerji and S. Bals, *Ultramicroscopy*, 2013, **127**, 40–47.

33 D. L. Chen, B. Goris, F. Bleichrodt, H. H. Mezerji, S. Bals, K. J. Batenburg, G. de With and H. Friedrich, *Ultramicroscopy*, 2014, **147**, 137–148.

34 J. D. Roehling, K. J. Batenburg, F. B. Swain, A. J. Moule and I. Arslan, *Adv. Funct. Mater.*, 2013, **23**, 2115–2122.

614 | *Energy Environ. Sci.*, 2020, **13**, 601–615

This journal is © The Royal Society of Chemistry 2020

35 B. S. S. Pokuri, J. Sit, O. Wodo, D. Baran, T. Ameri, C. J. Brabec, A. J. Moule and B. Ganapathysubramanian, *Adv. Energy Mater.*, 2017, **7**, 1701269.

36 O. Wodo, J. D. Roehling, A. J. Moule and B. Ganapathysubramanian, *Energy Environ. Sci.*, 2013, **6**, 3060–3070.

37 N. Tessler, Y. Preezant, N. Rappaport and Y. Roichman, *Adv. Mater.*, 2009, **21**, 2741–2761.

38 L. Demeyu, S. Stafstroem and M. Bekele, *Phys. Rev. B: Condens. Matter Mater. Phys.*, 2007, **76**, 155202.

39 J. J. Kwiatkowski, J. M. Frost and J. Nelson, *Nano Lett.*, 2009, **9**, 1085–1090.

40 A. Sharma, F. W. A. van Oost, M. Kemerink and P. A. Bobbert, *Phys. Rev. B: Condens. Matter Mater. Phys.*, 2012, **85**, 235302.

41 L. Y. Meng, Y. Shang, Q. K. Li, Y. F. Li, X. W. Zhan, Z. G. Shuai, R. G. E. Kimber and A. B. Walker, *J. Phys. Chem. B*, 2010, **114**, 36–41.

42 C. Groves, *Energy Environ. Sci.*, 2013, **6**, 3202–3217.

43 M. Mesta, M. Carvelli, R. J. de Vries, H. van Eersel, J. J. M. van der Holst, M. Schober, M. Furno, B. Lüssem, K. Leo, P. Loebl, R. Coehoorn and P. A. Bobbert, *Nat. Mater.*, 2013, **12**, 652–658.

44 R. Coehoorn, H. van Eersel, P. Bobbert and R. Janssen, *Adv. Funct. Mater.*, 2015, **25**, 2024–2037.

45 H. van Eersel, P. A. Bobbert, R. A. J. Janssen and R. Coehoorn, *Appl. Phys. Lett.*, 2014, **105**, 143303.

46 Y. F. Shen and N. C. Giebink, *Phys. Rev. Appl.*, 2015, **4**, 054017.

47 H. Abdalla, S. Fabiano and M. Kemerink, *Phys. Rev. B*, 2017, **95**, 085301.

48 J. Nelson, J. J. Kwiatkowski, J. Kirkpatrick and J. M. Frost, *Acc. Chem. Res.*, 2009, **42**, 1768–1778.

49 H. Y. Li, L. Duan, D. Q. Zhang, G. F. Dong, J. Qiao, L. D. Wang and Y. Qiu, *J. Phys. Chem. C*, 2014, **118**, 6052–6058.

50 H. Y. Li, Y. Qiu and L. Duan, *Org. Electron.*, 2016, **33**, 164–171.

51 H. Y. Li and J.-L. Brédas, *Adv. Funct. Mater.*, 2018, **28**, 1801460.

52 C. Groves, R. G. E. Kimber and A. B. Walker, *J. Chem. Phys.*, 2010, **133**, 144110.

53 D. R. Kozub, K. Vakhshouri, L. M. Orme, C. Wang, A. Hexemer and E. D. Gomez, *Macromolecules*, 2011, **44**, 5722–5726.

54 K. Vakhshouri, D. R. Kozub, C. Wang, A. Salleo and E. D. Gomez, *Phys. Rev. Lett.*, 2012, **108**, 026601.

55 N. K. Elumalai and A. Uddin, *Energy Environ. Sci.*, 2016, **9**, 391–410.

56 W. Xu, C. Yi, X. Yao, L. Jiang, X. Gong and Y. Cao, *ACS Omega*, 2017, **2**, 1786–1794.

57 Z. G. Yu, D. L. Smith, A. Saxena, R. L. Martin and A. R. Bishop, *Phys. Rev. Lett.*, 2000, **84**, 721–724.

58 Z. G. Yu, D. L. Smith, A. Saxena, R. L. Martin and A. R. Bishop, *Phys. Rev. B: Condens. Matter Mater. Phys.*, 2001, **63**, 085202.

59 W. F. Pasveer, J. Cottaar, C. Tanase, R. Coehoorn, P. A. Bobbert, P. W. M. Blom, D. M. de Leeuw and M. A. J. Michels, *Phys. Rev. Lett.*, 2005, **94**, 206601.

60 J. J. M. van der Holst, M. A. Uijttewaal, B. Ramachandhran, R. Coehoorn, P. A. Bobbert, G. A. de Wijs and R. A. de Groot, *Phys. Rev. B: Condens. Matter Mater. Phys.*, 2009, **79**, 085203.

61 L. J. A. Koster, *Phys. Rev. B: Condens. Matter Mater. Phys.*, 2010, **81**, 205318.

62 F. Liu, J. Lin, T. Manaka and M. Iwamoto, *J. Appl. Phys.*, 2011, **109**, 104512.

63 M. Z. Szymanski, B. Luszczynska and D. Djurado, *IEEE J. Sel. Top. Quantum Electron.*, 2013, **19**, 7800107.

64 A. Miller and E. Abrahams, *Phys. Rev.*, 1960, **120**, 745–755.

65 H. Y. Li and J.-L. Brédas, *J. Phys. Chem. Lett.*, 2017, **8**, 2507–2512.

66 J. Miao, H. Chen, F. Liu, B. Zhao, L. Hu, Z. He and H. Wu, *Appl. Phys. Lett.*, 2015, **106**, 183302.

67 M. A. Lampert and P. Mark, *Current injection in solids*, Academic Press, New York, 1970.

68 I. Lange, J. Kniepert, P. Pingel, I. Dumsch, S. Allard, S. Janietz, U. Scherf and D. Neher, *J. Phys. Chem. Lett.*, 2013, **4**, 3865–3871.

69 H. Y. Li, Y. Li, H. Li and J.-L. Brédas, *Adv. Funct. Mater.*, 2017, **27**, 1605715.

70 E. Tutis, D. Berner and L. Zuppiroli, *J. Appl. Phys.*, 2003, **93**, 4594–4602.

71 S. L. M. van Mensfoort and R. Coehoorn, *Phys. Rev. B: Condens. Matter Mater. Phys.*, 2008, **78**, 085207.

72 H. Y. Li, L. Duan, D. Q. Zhang and Y. Qiu, *J. Phys. Chem. C*, 2014, **118**, 9990–9995.

73 Y. Roichman, Y. Preezant and N. Tessler, *Phys. Status Solidi A*, 2004, **201**, 1246–1262.

74 S. A. Mauger, L. Chang, S. Friedrich, C. W. Rochester, D. M. Huang, P. Wang and A. J. Moulé, *Adv. Funct. Mater.*, 2013, **23**, 1935–1946.

75 R. Chintala, J. G. Tait, P. Eyben, E. Voroshazi, S. Surana, C. Fleischmann, T. Conard and W. Vandervorst, *Nanoscale*, 2016, **8**, 3629–3637.

76 D. S. Germack, C. K. Chan, R. J. Kline, D. A. Fischer, D. J. Gundlach, M. F. Toney, L. J. Richter and D. M. DeLongchamp, *Macromolecules*, 2010, **43**, 3828–3836.

77 D. S. Germack, C. K. Chan, B. H. Hamadani, L. J. Richter, D. A. Fischer, D. J. Gundlach and D. M. DeLongchamp, *Appl. Phys. Lett.*, 2009, **94**, 233303.

78 C. Göhler, A. Wagenpfahl and C. Deibel, *Adv. Electron. Mater.*, 2018, **4**, 1700505.

This journal is © The Royal Society of Chemistry 2020

Energy Environ. Sci., 2020, **13**, 601–615 | 615